Foundering Lithosphere Imaged Beneath the Southern Sierra Nevada, California, USA

Oliver S. Boyd,* Craig H. Jones, Anne F. Sheehan

Seismic tomography reveals garnet-rich crust and mantle lithosphere descending into the upper mantle beneath the southeastern Sierra Nevada. The descending lithosphere consists of two layers: an iron-rich eclogite above a magnesium-rich garnet peridotite. These results place descending eclogite above and east of high *P* wave speed material previously imaged beneath the southern Great Valley, suggesting a previously unsuspected coherence in the lithospheric removal process.

The Sierra Nevada mountain range of California is one of the highest (about 3 km mean elevation) in the United States; however, the crust is only 35 km thick (1) and requires some unusual structure in the mantle. Xenoliths (2) and volcanic rocks (3, 4) suggest that the upper mantle source for these materials, beneath the Sierra Nevada, changed from an eclogite facies garnet pyroxenite to a garnet-free spinel peridotite about 4 million years ago (Ma). Eclogitic rocks may still be present in the upper mantle below the Sierra Nevada (5), and knowing where and how much is left constrains how lithospheric material is removed and how continental crust grows and changes beneath mountain ranges (6). To determine whether there are any eclogitic rocks left, we used three-dimensional models of *P* and *S* wave speeds to define compositional and thermal characteristics of the lithosphere. We measured attenuation to correct the velocities for anelastic effects, which include temperature and hydration. The corrected wave speeds are subsequently termed anharmonic wave speeds and compared with laboratory predictions.

Low Pn velocities directly beneath the high Sierra (7, 8) and high attenuation in the upper mantle in the region (9) are consistent with high temperature, low-density material. Shear wave splitting measurements determined from the seismic phase SKS (10, 11) (Fig. 1) indicate strong seismic anisotropy oriented N80°E beneath the central Sierra, probably because of the presence of strained, olivine-rich, peridotitic mantle. Less splitting beneath the eastern and western Sierra may indicate largely isotropic material, such as eclogite (12), little strain, or a vertical fast axis of anisotropy. The region of large SKS splitting and low Pn velocity correlates well with high mantle electrical conduc-

tivity that is probably due to 1% partial melt beneath the southern Sierra Nevada (13). These observations are consistent with the presence of a peridotitic uppermost mantle near asthenospheric temperatures near the Sierran crest today.

We recorded 40 teleseismic events that yielded 800 seismic wave traces on 24 broadband seismometers (Fig. 1). We measured

direct *P* wave and S_{fast} and S_{slow} wave travel time delays (t_P, t_{S_f}, and t_{S_s}) and S_{fast} and S_{slow} wave path–integrated attenuation, Δt^* (14), to invert for variations in *P* wave speed, v_P, fast and slow *S* wave speeds (v_{S_f} and v_{S_s}), and fast- and slow-oriented *S* wave attenuation ($Q_{S_f}^{-1}$ and $Q_{S_s}^{-1}$). These were combined to examine variations in the ratio of *P* wave to *S* wave velocity, v_P/v_S, and transverse *S* wave anisotropy. Our tomographic inversions reduce the variance of the data by more than half of that available, whereas measurement noise and station and event statics account for the remainder (15).

The tomographic models reveal regions of alternating high and low velocity and attenuation that dip ~55° to the east southeast (Fig. 2). The region of high *P* wave velocity at 36.4°N extends from –119.5°W to –118°W and may be what has been referred to as the Isabella anomaly. The volume above this anomaly consists of a slow *P* and *S* wave region. The *S* wave velocities decrease more across this contrast than do the *P* wave velocities, giving rise to an increase in the v_P/v_S ratio. These seismic anomalies trend northeast (Fig. 3C).
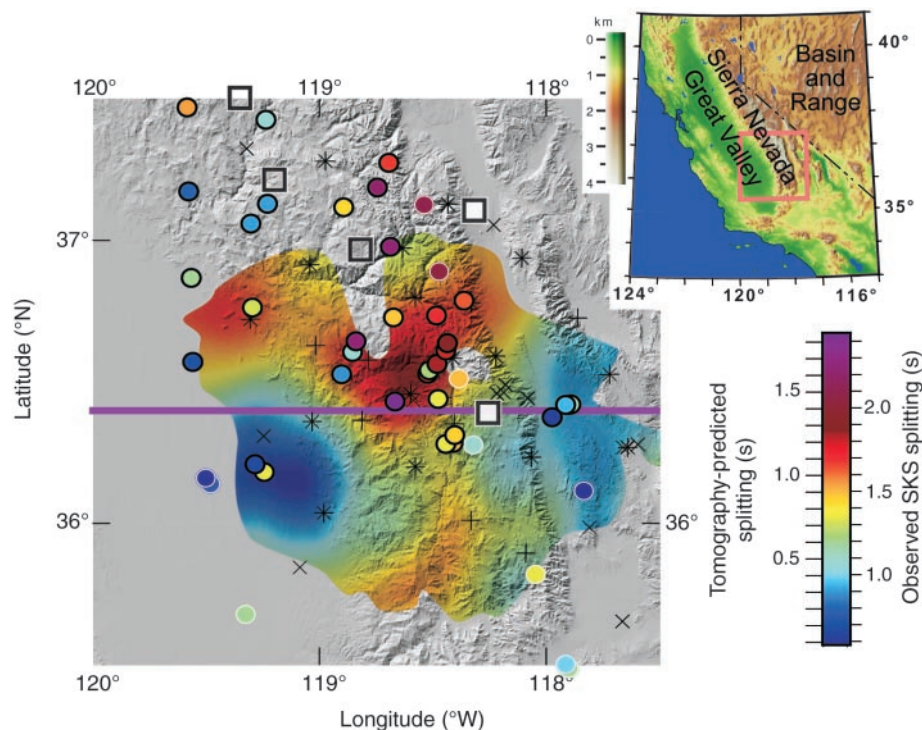
Fig. 1. Topographic map of the southern Sierra Nevada overlain with tomographically predicted shear wave splitting (this study) and independently determined SKS splitting measurements, filled circles with white (10) or black (11) outline. Map of Nevada and California with pink outline of study area given in the upper right for reference. The SKS measurements are placed at 125-km depth along the SKS ray path. The tomographically predicted splitting time is determined by integrating differences between the fast and slow *S* wave speed models in the upper 200 km for regions with greater than 150-km thickness of resolution greater than 0.5. Thick purple line crossing at 36.4°N is the latitudinal position of the vertical slices in Fig. 2. The plus symbols are seismograph stations used for the tomography, the multiplication symbols are stations used to measure SKS splitting, and the asterisks, plus symbols overlain by multiplication symbols, are stations used for both tomography and SKS splitting. The open boxes are garnet peridotite and garnet pyroxenite xenolith localities; solid boxes are spinel peridotite xenolith localities.

Department of Geological Sciences, University of Colorado at Boulder, 2200 Colorado Avenue, Boulder, CO 80309–0399, USA.

*To whom correspondence should be addressed. E-mail: oliver.boyd@colorado.edu

Upon vertically integrating the differences in S_{fast} and S_{slow} travel times for the top 200 km, we are able explain more than 50% of the variance of the SKS splitting measurements (Fig. 1 and fig. S1) (15), an independent verification of our subsurface distribution in anisotropy. The SKS measurements were not used in the inversion; we used only the orientation of fast S wave speed derived from the splitting analysis. The shallow depth for the origin of the splitting (<200 km) is consistent with the 1-s variation in splitting amplitudes over short distances (<50 km) and inconsistent with splitting distributed over greater depths.

Attenuation is needed to distinguish between the effects on wave speed from thermal and compositional variations (16, 17). Anisotropy (12) and Poisson's ratio (18) can then be used to constrain the composi-

tion (Table 1). Because of anelasticity, temperature variations will cause seismic velocities and attenuation to vary predictably (19). We interpret deviations from the thermal relationship as being caused by variations in composition.

Because the dipping layer of low wave speeds is accompanied by low attenuation, temperatures are relatively low (~200 K lower than the material to the east), and partial melt or partially water-saturated minerals are not likely present. This leaves some sort of compositional effect producing, in addition to low velocities, a high v_P/v_S ratio and variable anisotropy. High v_P/v_S ratios can indicate an increase in the amount of pyroxene and garnet relative to olivine or a decrease in the Mg number [Mg/(Mg + Fe)]. The variable anisotropy is more difficult to interpret. Lower

anisotropies can be from an absence of olivine, an absence of strain, or a heterogeneously strained peridotite. In response to infilling asthenosphere, the low anisotropy in the inferred region of spinel peridotite (Fig. 2D) could be anisotropic but have a near-vertical axis of orientation. Normally isotropic lithologies like eclogites might be anisotropic if pervasively cut by dikes or if the pyroxenes have become preferentially aligned (15). The large anisotropy appearing below the dipping layer of high P wave velocities may reflect lateral extrusion of asthenospheric peridotite in response to delaminating mantle lithosphere.

Ambiguity in interpreting the tomographic results can be reduced by examining the xenoliths erupted nearby in the central Sierra Nevada. There are three groups of xenoliths: garnet pyroxenites and garnet peridotites (both erupted before 8 Ma) constituting the old mantle lithosphere (2, 20) and fertile, olivine-rich, garnet-free spinel peridotites (erupted since 4 Ma) with an asthenospheric affinity (2). Chemically, the garnet and pyroxene in the pyroxenites tend to have low Mg, whereas the olivine in the peridotites has a higher Mg number (2). This observation means that the garnet pyroxenite will have higher v_P/v_S ratios relative to the peridotites.

We calculated the P and S wave speeds (15, 21) for a range of expected compositions and compare these values to our observations of anharmonic wave speed (15) to broadly determine the mineralogy and Mg numbers in the observed seismic anomalies (Fig. 3). The modal proportions for the garnet pyroxenite xenolith samples are predicted to be about 65% clinopyroxene and 35% garnet (22). The Mg number ranges from 0.6 to 0.9 for the clinopyroxenes and 0.3 to 0.6 for the garnet (2). The composition that best matches our seismic observations averages 70% pyroxene and 30% garnet (15). Compositions having as much as 40% garnet would be acceptable if a Reuss average, as opposed to the Voight-Reuss-Hill average (23) used here, is favored. One garnet peridotite sample has 75% olivine, 15% orthopyroxene, 5% clinopyroxene, and 5% garnet (24), whereas the Mg numbers are reported to be on average 0.91, 0.91, 0.92, and 0.85 for those minerals, respectively (2). Our seismically determined composition averages 75% olivine, 20% pyroxene, and 5% garnet. The young peridotite samples are devoid of garnet and average 80% olivine, with the remainder orthopyroxene, clinopyroxene, and spinel (25). Their Mg numbers average 0.89, 0.89, 0.87, and 0.67, respectively (2). Because a majority of the young samples have been classified as harzburgites, we restrict our analysis to clinopyroxene-free assemblages. We find this composition has on average 80% olivine, 16% pyroxene, and 4% garnet (26).
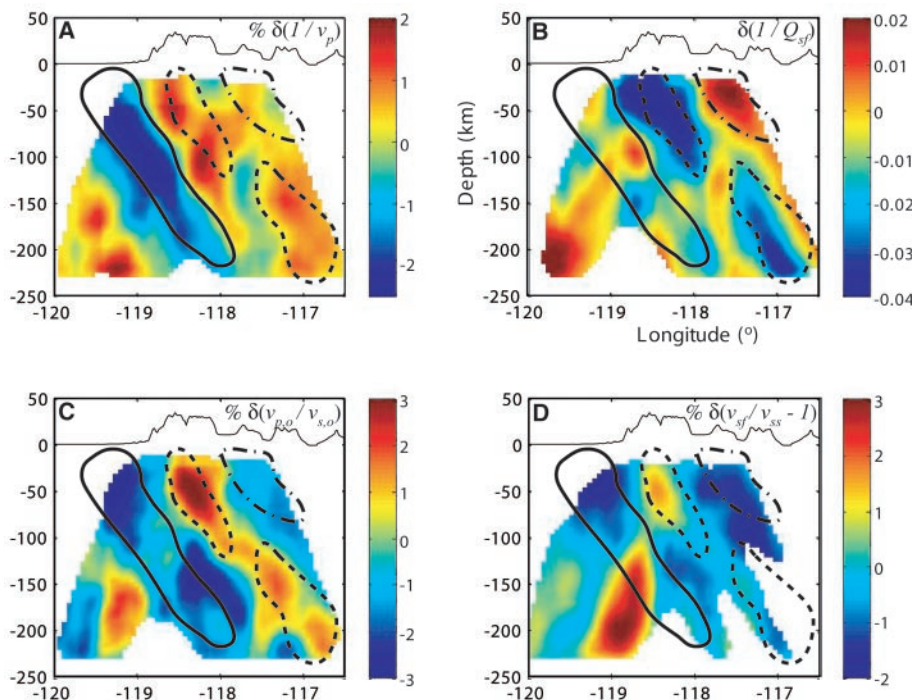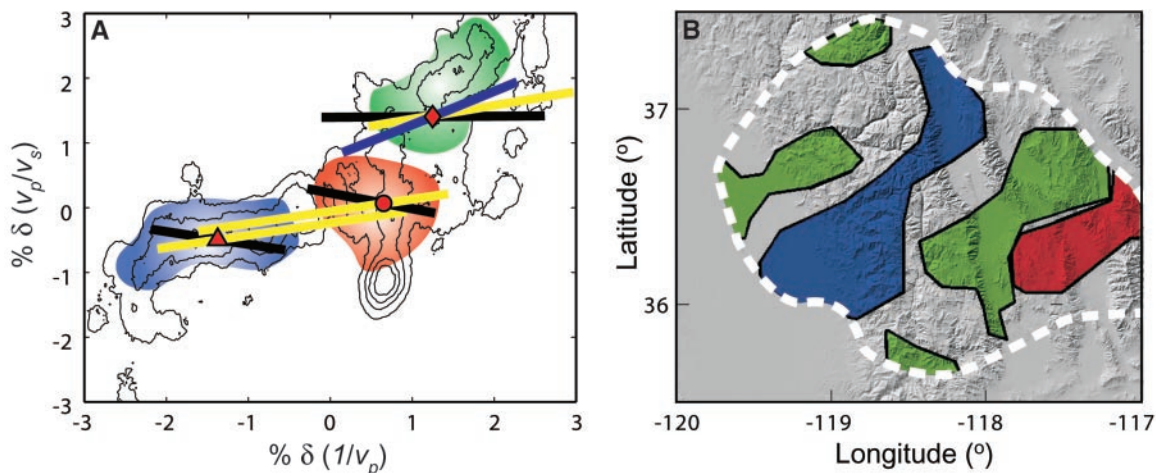

Fig. 2. Vertical slices of our tomographic models and derived quantities: percent change in P wave slowness (**A**), change in attenuation (**B**), percent change in anharmonic v_P/v_S ratio where v_S is taken from the average of the fast and slow models (**C**), and shear wave anisotropy where the slow model is derived as residuals from the fast model (**D**). The solid lines indicate regions of descending garnet peridotite, and the dashed lines delineate regions of garnet pyroxenite. The regions of low velocities and high attenuation above the garnet pyroxenite are presumably the infilling of asthenospheric spinel peridotite (dashed-dot outlines). Topography is depicted with 10 times vertical exaggeration.

Table 1. Changes observed in geophysical properties in the mantle from different causes. The asterisk indicates that the attenuation will only increase if high temperatures are required to produce melt (15). The question mark indicates that anisotropy may increase or change orientation if melt pockets and/or bands are favorably oriented.

Increasing factor	v_P	v_P/v_S	Attenuation	Anisotropy	Density
Temperature	Decrease	Increase	Increase	No change	Decrease
Melt	Decrease	Increase	*	?	Decrease
Magnesium	Increase	Decrease	No change	No change	Decrease
Garnet/olivine ratio	Increase	Increase	No change	Decrease	Increase

Fig. 3. (**A**) Percent change in anharmonic v_P/v_S ratio versus percent change in anharmonic *P* wave slowness for a range of model compositions at a pressure of 3 GPa and a range of temperatures. Compositions defined in the text that best match the seismic observations are garnet pyroxenite (red diamond) at 1200°C, spinel peridotite (red circle) at 2000°C, and garnet peridotite (red triangle) at 1000°C. Thick black lines represent ranges in composition where garnet is substituted for pyroxene. For the garnet pyroxenite, garnet varies from 20% (right end of black line, slower wave speeds) to 40%; the spinel peridotite, 0 to 10%; and the garnet peridotite, 0 to 10%. Yellow lines represent a 400 K variation in temperature (900 to 1300°C), with faster wave speeds (to the left) accompanying lower temperatures. The blue line spans the range of Mg numbers for the garnet pyroxenite samples. Contours denote anharmonic *P* wave slowness and v_P/v_S from our Sierran tomography from 75- to 100-km depth. Each contour interval represents 20% of the data. Colored areas correspond to compositional regions outlined in the tomography of Fig. 2 and shaded areas in the 100-km-depth slice (**B**). Garnet pyroxenite, green; spinel peridotite, red; and garnet peridotite, blue. Compositional zones in (B) derived from tomography using composition relations (*15*) with *P* wave slowness, Poisson's ratio, anisotropy, and attenuation. The white dashed line delimits the part of the tomography model with resolution greater than 0.4.

Many eclogites are seismically fast because they have a large proportion of garnet and much of the pyroxene is in the form of jadeite (*27*). The xenoliths found here, however, have large amounts of clinopyroxene (*24*) and very little jadeite (*2*). The garnet pyroxenites are therefore slower than common eclogites and have a higher v_P/v_S ratio relative to the peridotites (Fig. 3A). A comparison of the characteristics of the seismic anomalies to calculated values for mineral assemblages (Fig. 3A) reveals that the dipping layer of high velocity is the garnet peridotite; the low velocity layer above, garnet pyroxenite; and the seismically intermediate region above and to the east, asthenospheric spinel peridotite (Fig. 2). A map view of the older garnet-bearing assemblages at 100-km depth indicates a northeast strike to this structure (Fig. 3B). The seismically determined compositions imply that, at 100-km depth, densities increase from close to neutrally buoyant garnet peridotite below to very dense, negatively buoyant ($\Delta\rho \approx 185$ kg/m^3) garnet pyroxenite above.

Although we have suggested specific differences in composition and temperature for the three rock assemblages identified, the most robust conclusion is that three distinct rock types exist in the upper mantle beneath the Sierra Nevada. This observation is made possible by correcting measured *P* and *S* wave seismic velocities for attenuation and comparing these values to laboratory results. The apparent dip of the two garnet-bearing packages and the asymmetry of the package (garnet peridotite to the west of the garnet pyroxenite) are important constraints on the mechanism of removal of this material. The asymmetry resembles delamination of stratified mantle lithosphere from the crust and is inconsistent with most numerical models of removal by development of a Rayleigh-Taylor instability (*28*), although such asymmetry might be produced by an initially asymmetric instability (*29*). The eastward plunge of this body indicates that either material has moved directly downward or somewhat to the east relative to the overlying crust, in contrast to motion to the west relative to the crust inferred from older images of this structure (*5*). Imaging one of the very few (if not the only) examples of ongoing removal of mantle lithosphere from beneath continental crust, this tomography provides some of the best observational constraints on the process of removing dense material from continental crust.

References and Notes

1. B. Wernicke *et al.*, *Science* **271**, 190 (1996).
2. M. Ducea, J. Saleeby, *J. Geophys. Res.* **101**, 8229 (1996).
3. C. R. Manley, A. F. Glazner, G. L. Farmer, *Geology* **28**, 811 (2000).
4. G. L. Farmer, A. F. Glazner, C. R. Manley, *Geol. Soc. Am. Bull.* **114**, 754 (2002).
5. G. Zandt, *Int. Geol. Rev.* **45**, 213 (2003).
6. M. Ducea, *J. Geophys. Res.* **107**, 10.1029/2001JB000643 (2002).
7. C. H. Jones, H. Kanamori, S. W. Roecker, *J. Geophys. Res.* **99**, 4567 (1994).
8. M. M. Fliedner *et al.*, *Geology* **24**, 367 (1996).
9. H. H. Al-Khatib, B. J. Mitchell, *J. Geophys. Res.* **96**, 18129 (1991).
10. J. Polet, H. Kanamori, *Geophys. J. Int.* **149**, 313 (2002).
11. C. H. Jones, R. A. Phinney, *Geol. Soc. Am. Abstr. Prog.* **31** (no. 7), A-481 (1999).
12. N. I. Christensen, W. D. Mooney, *J. Geophys. Res.* **100**, 9761 (1995).
13. M. Ducea, S. K. Park, *Geophys. Res. Lett.* **27**, 2405 (2000).
14. A. F. Sheehan, S. C. Solomon, *J. Geophys. Res.* **97**, 15339 (1992).
15. Please refer to the supporting online material on *Science* Online for more information about seismic methods, resolution, and calculation of mineral properties.
16. O. S. Boyd, A. F. Sheehan, in *Lithospheric Structure and Evolution of the Rocky Mountain Region*, K. E. Karlstrom, G. R. Keller, Eds. (*Geophys. Monogr. Am. Geophys. Union*), in press.
17. S. Karato, *Geophys. Res. Lett.* **20**, 1623 (1993).
18. N. I. Christensen, *J. Geophys. Res.* **101**, 3139 (1996).
19. I. Jackson, *Annu. Rev. Earth Planet. Sci.* **21**, 375 (1993).
20. F. C. W. Dodge, J. P. Lockwood, L. C. Calk, *Geol. Soc. Am. Bull.* **100**, 938 (1988).
21. B. R. Hacker, G. A. Abers, *Geochem. Geophys. Geosys.* **5**, 10.1029/2003GC000614 (2004).
22. J. Saleeby, M. Ducea, D. Clemens-Knott, *Tectonics* **22**, 10.1029/2002TC001374 (2003).
23. J. P. Watt, G. F. Davies, J. O'Connell, *Rev. Geophys. Space Phys.* **14**, 541 (1976).
24. M. Ducea, J. Saleeby, *Contrib. Mineral. Petrol.* **133**, 169 (1998).
25. H. G. Wilshire *et al.*, *U.S. Geol. Surv. Prof. Pap. 1443* (1988), p. 179.
26. Garnet is used for the spinel peridotite composition because we are considering seismic velocities at 3 GPa, by which pressure spinel would have transformed to garnet.
27. R. G. Coleman, D. E. Lee, J. B. Beatty, W. W. Brannock, *Geol. Soc. Am. Bull.* **76**, 483 (1965).
28. G. A. Houseman, P. Molnar, *Geophys. J. Int.* **128**, 125 (1997).
29. M. Jull, P. B. Kelemen, *J. Geophys. Res.* **106**, 6423 (2001).
30. Thanks to P. Molnar and L. Farmer for helpful discussion and B. Phinney and several land use agencies (U.S. Forest Service, Sequoia and Kings Canyon National Parks, and Bureau of Land Management) for help in obtaining the data. We also acknowledge two anonymous reviewers and L. Rowan for thorough reviews. This work was supported by NSF grants 9526974 and 0003747 and a Cooperative Institute for Research in Environmental Research Sciences fellowship.

Foundering Lithosphere Imaged Beneath the Southern Sierra Nevada, California, USA

1) Method

The network of 24 broadband seismometers comprising the seismological component of the Sierran Paradox Experiment was deployed from late May to mid October 1997 (Fig. 1, Table S1). Stations were approximately 20 km apart spanning an area of nearly 3 x 10^4 km^2. Approximately 40 teleseismic events of appropriate distance range and magnitude for this study yielded 800 seismic traces to measure (Table S2). We have measured direct P, S_{fast}, and S_{slow}-wave travel time delays, t_p, t_{sf}, and t_{ss}, and S_{fast}-wave path integrated attenuation, Δt^*, to invert for variations in P-wave velocity, v_p, the ratio of P-wave to S-wave velocity, v_p/v_s, %S anisotropy, and S_{fast}-wave attenuation, Q^{-1}_s.

S-wave delay times are measured using the fast (N80°E) and slow (N10°W) components of motion as determined from SKS shear-wave splitting measurements (*S1*) and facilitates an appreciation for the depth dependence of anisotropy. Relative travel times are measured by cross-correlating waveforms that have been bandpass filtered from 1 to 100 seconds; across the array the shapes of teleseismic arrivals are found to vary only slightly and cross-correlation should give reliable measurements of differential arrival times.

The horizontal channels are rotated into the fast and slow directions prior to measuring spectral ratios. A straight line is fit to the spectral ratio between 10 and 30 seconds to derive Δt^* (*S2*). Rotating into the fast and slow directions keeps the second wavelet due to splitting from interfering with the primary wavelet's spectra, thereby reducing Δt^* error (*S2*). No other correction for Δt^* is made, as is evident by the low variance reduction attained by the differential attenuation tomographic model (~25%). This value is low but much greater than a previous study in which 10% variance reduction was shown to be adequate to resolve subsurface features. Boyd and Sheehan (*S2*) show that interference from basin reverberations, anisotropy, and other forms of scattering can lead to significant errors in Δt^*. They also point out that if uncorrelated, these uncertainties will cancel and a meaningful differential attenuation tomographic model can be obtained. The effect of focusing and defocusing on Δt^* is expected to be small based on the location, extent and magnitude of the velocity anomalies (*S2*).

Inversion of the P and S-wave differential travel times and S-wave Δt^* to produce the tomographic models of differential slowness and attenuation is performed according to the integral equations

$$
\partial t_x = \int \partial \frac{1}{v_x} dl
$$
$$
\partial t_x^* = \int \partial \frac{1}{v_x Q_x} dl
$$

(S1)

where the subscript x represents either the P (for velocity), S_{slow}, or S_{fast} waves. The distances spent along the ray path are given by dl. In our method, a primary block size of 50 km is chosen because it has sufficient ray density to produce a good average. We perform an inversion using weighted singular value decomposition where the weights are the inverse of the standard errors for each measurement derived from the signal to noise ratio of the waveforms. The blocks are translated 5 km until inversions are obtained for all possible translations generating a total of 10 x 10 x 10 or 1000 inversions. They are sequentially combined and subsequently convolved with a 25 km cube to produce a smooth tomographic model (*S2*). We iterate the inversions four times using the residuals relative to the previous iteration as input data. The residuals are defined as the original data minus the predicted data minus the station statics. After four iterations there is little improvement in variance reduction.

We derived the S_{slow}-wave tomographic model from residuals relative to both a one dimensional velocity model for tectonic North America (*S3*) and from the final S_{fast} model (Fig. 2d). In both cases, the same general patterns of anisotropy emerge, and the variance reductions are similar. The resulting anisotropic model predicts splitting that is very similar to independent SKS splitting measurements (Fig 1, Fig. S1). Tomographically predicted splitting reduces the variance of the SKS measurements by more than 50%. A linear regression to the data presented in figure S1 results in a slope of 0.95 ± 0.1, y-intercept of 0.42 ± 0.07, and linear correlation coefficient of 0.7. The intercept is non-zero because our study has solved for relative differences in velocity and we have assumed the smallest anisotropy in our tomographic model is zero.

Event and station statics (Table S1) also contribute to differential travel times and Δt^*. The event static is accounted for by first demeaning the measurements for a given event and then including a solution for the event static in the inversion. We find that the event statics resulting from the solution in the inversion are negligible, much less than 1% of the total variance for all models.

For the case of seismic velocity, station statics are obtained initially by correcting for elevation, before inversion, assuming a constant P and S-wave velocity and then, after inversion, examining the difference between the mean observed station delay relative to the mean predicted station delay. After the elevation corrections have been applied and four iterations of the inversions have been performed, removing the mean delay at each station removes an additional 20% of the original variance in arrival times. These static corrections are consistent with variations in crustal velocity, slow in the Sierra and faster to the east and west (*S4*). Stations statics for Δt^* account for less than 10% of the measured variance.

The total variance reductions from our tomographic inversions are 60% (∂v_p^{-1}), 64% (∂v_{sf}^{-1}), 61%, (∂v_{ss}^{-1}), 30%, (∂Q_{sf}^{-1}), and 21% (∂Q_{ss}^{-1}). Much of the variance that has not been accounted for is likely due to higher spatial frequency variations in velocity and attenuation as well as variability occurring outside of the model domain. The substantially lower variance reductions for differential attenuation are due to the additional sources of uncertainty in Δt^*. Uncertainty in the measurements was determined by adding noise to the source time series and observing its effect on the measurement. The signal to noise ratio of the real times series was then correlated to the signal to noise

4

ratio of the synthetic time series to determine the uncertainty. Variance due to this uncertainty in the measurements approach 4% (∂v_p^{-1}), 18% (∂v_{sf}^{-1}), 15% (∂v_{ss}^{-1}), 57% (∂Q_{sf}^{-1}), and 59% (∂Q_{ss}^{-1}), indicating that we have not overfit our observations but have recovered most of the variation from lateral variations in structure.

Calculation of anharmonic wave speeds requires absolute attenuation. Since we are interested in differences in wave speed, the exact offset of attenuation is not critical and so we safely add the minimum attenuation in our tomographic model to the attenuation values that are used to derive the anharmonic wave speeds. The correction for anelasticity involves the removal of the effects of dispersion from the seismic velocities. The correction is

$$V_0 = V\left[1 - \frac{1}{2}\cos\left(\frac{\pi\alpha}{2}\right)Q^{-1} \right]^{-1} \tag{S2}$$

where α reflects the frequency dependence of attenuation, assumed to be 0.25, and Q^{-1} is the seismic attenuation (*S5*). P-wave attenuation is assumed to be 4/9 S-wave attenuation, e.g. all energy is lost in shear. Since $Q \propto w^{0.25}$ and most of the energy in the P-wave is closer to 1 second whereas it is closer to 20 seconds for the S wave, P-wave attenuation is additionally reduced by a factor of 2.1 ($(20/1)^{0.25}$).

The aerial extent of various compositions depicted in figure 3B was found using a number of seismic factors. The garnet peridotite was simply found by locating all fast anharmonic P-wave speeds and low anharmonic P-wave to S-wave speed ratios. Garnet

5

pyroxenite was almost as simple, slow anharmonic P-wave speeds and high anharmonic P-wave to S-wave speed ratios, but also includes the constraint of low attenuation. Spinel peridotite proved to be the most difficult to locate where in addition to subsetting on intermediate anharmonic P-wave speeds and P-wave to S-wave speed ratios, we used the constraint of low anisotropy.

2) Model resolution and fidelity

We conducted spike tests to verify the anomalies observed in our tomographic models. For the spike test, a 50 km cube was centered at 36.4°N, 118.5°W, and 100 km depth and given anomalous seismic parameters of -0.01 ($d(1/v_p)$), -0.02 ($d(1/v_{sf})$), 0.02 ($d(1/v_{ss})$), and -0.04 ($d(1/Q_{sf})$). The input anomalies result in derived anomalies of 1.80 ($v_{p,o}/v_{sf,o}$) relative to a background of 1.73 and 0.10 for fractional anisotropy (Fig. S3). The recovered amplitudes of these anomalies are -0.006 ($d(1/v_p)$), -0.014 ($d(1/v_{sf})$), 0.004 ($d(1/v_{ss})$), -0.04 ($d(1/Q_{sf})$) 1.78 ($v_{p,o}/v_{sf,o}$) and 0.05 (fractional anisotropy). The variance reductions for the primary models are 85% ($d(1/v_p)$), 92% ($d(1/v_{sf})$), 74% ($d(1/v_{ss})$), and 91% ($d(1/Q_{sf})$). The variance reductions, having values less than 100%, are due to imperfect ray coverage and the inability of the inversion to recover the strong seismic gradients near the spike edge. The discrepancy between the large variance reductions of these synthetic models relative to the real models is due to measurement uncertainty and noise.

Figure S2 contains the same vertical slice as Figure 2 of the main text and goes through the center of the synthetic anomaly. The seismic anomalies are well recovered

6

with the exception of the shear velocity oriented in the slow direction (Fig. S3). This is due to relatively poor ray coverage for the slow oriented shear wave at this latitude. As a consequence, the magnitude of the derived parameter of seismic anisotropy at this latitude is not well resolved.

The spike tests have similar features for each parameter. The spike should appear as a square but has been elongated in the vertical direction. There is also a small amount of smearing along the NW/SE and NE/SW ray path directions. These artifacts do not reproduce the geometry of the features seen in the tomographic slices presented in Figure 2 which cover the entire depth range and trend more E-W. In addition, the dipping high velocity feature does not have stations projected along its axis to the surface, a verification that it is not an effect of smearing of an anomaly along a ray path.

The reason there is varying ray coverage for each S-wave observable is because of the weighting. Each data point and corresponding ray are weighted according to the standard error of the measurement which is a function of the signal to noise ratio. S-waves are polarized differently for each event, so when rotated into S_{fast} and S_{slow} coordinates, one component will often have a small amplitude. It happens that the component of the S-wave in the slow direction usually has a greater amount of noise and hence less weight for paths that traverse this region.

7

3) Effects on wavespeed and calculation of mineral physics constants

Decreases in velocity can be caused by increases in temperature (*S6*), the presence of partial melt (*S7*), the presence of partially saturated nominally anhydrous minerals (*S8*), or petrological and geochemical effects such as differing amounts of garnet relative to olivine or magnesium relative to iron (*S9*). Of course, these possibilities also affect v_p/v_s, attenuation, and anisotropy (Table 1). Partial melt in itself may not affect attenuation (*S10*) but will significantly decrease the P and S wavespeeds and lead to greater v_p/v_s ratios. Attenuation will probably increase if melt is present but only because of the increased temperatures needed to produce melt. It is possible that low attenuation could accompany partial melt if there are mineral phases present that melt at lower temperatures (*S2*). The effect of saturating nominally anhydrous minerals with water would probably increase attenuation (*S8*), resulting in higher v_p/v_s ratios. Compositional effects will have a small effect on attenuation but a much greater effect on v_p/v_s ratios. For example, garnet is generally faster than olivine and has a greater v_p/v_s ratio. Increasing the Mg# [Mg/(Mg+Fe)] of most minerals increases the seismic velocities but decreases the v_p/v_s ratio (*S11*). Composition also significantly effects seismic anisotropy. Olivine is a highly anisotropic mineral (*S12*) while garnet is not (*S13*). Pyroxenes have significant anisotropy (*S14*) but are not expected to develop preferred mineral orientation and hence are not expected to contribute to anisotropy in the rock aggregate (*S15*). To interpret our results, we must account for this information in light of constraints provided by petrology of the xenoliths.

The mineral end-member modal compositions for the three average rock types appearing in figure 3A are as follows. They have the same Mg# as reported in the main text but relative amounts of pyroxene and garnet were adjusted to match the tomographically determined seismic velocities. The garnet pyroxenite consists of 15.5% almandine, 4.2% grossular, 10.3% pyrope, 50.7% diopside, and 19.3% hedenbergite. The garnet peridotite consists of 0.7% almandine, 0.7% grossular, 3.6% pyrope, 65.2% forsterite, 9.8% fayalite, 4.6% diopside, 13.3% enstatite, 1.7% ferrosilite, and 0.4% hedenbergite. Finally, the spinel peridotite, but substituting garnet for spinel since the calculations were made at 3GPa, consists of 1.5% almandine, 2.5% pyrope, 67.7 % forsterite, 12.3% fayalite, 13.8% enstatite, and 2.2% ferrosilite.

As stated in the article, the calculation of mineral physics constants is found using the methods of Bina and Hellfrich (*S16*) and Holland and Powell (*S17*) with the mineral constants compiled by Hacker and Abers (*S11*). The method is also summarized by Hacker and Abers (*S11*) though the equations for the temperature dependence of thermal expansion and the isothermal bulk modulus at elevated temperature and pressure were misprinted. These equations are correctly printed in a later article by Hacker and Abers (*S18*) in which they also include an Excel macro to perform this calculation. Our method differs slightly and is explained in the subsequent paragraphs.

The anharmonic P-wave and S-wave velocities are given by

$$v_p = \sqrt{\frac{K_S + \frac{4}{3}\mu}{\rho}}$$

$$v_s = \sqrt{\frac{\mu}{\rho}}$$

(S3)

where K_S is the adiabatic bulk modulus, μ is the shear modulus and ρ is the density. Changes to the density and moduli due to changes in temperature, dT, are related to the thermal expansivity, α, through

$$K_T(T) = K_{T0}e^{-\delta_T \int_{298}^{T} \alpha dT}$$

$$\mu(T) = \mu_0 e^{-\theta \int_{298}^{T} \alpha dT}$$

$$\rho(T) = \rho_0 e^{-\int_{298}^{T} \alpha dT}$$

(S4)

where δ_T is the isothermal second Gruneisen parameter, θ is the logarithmic change in shear modulus with respect to pressure, and K_T is the isothermal bulk modulus. The isothermal bulk modulus is related to the adiabatic bulk modulus by

$$K_S = K_T(1 + T\alpha\gamma_{th}).$$

(S5)

Here, γ_{th} is the first Gruneisen parameter. Before this equation can be implemented, the thermal expansivity and isothermal bulk modulus must be corrected for the change in

10

pressure and temperature. The integral over αdT can be solved easily given that α is approximately related to temperature by a simple polynomial

$$\alpha(T) = \alpha^o \left(1 - \frac{10}{\sqrt{T}} \right) \tag{S6}$$

where α^o is the high temperature limit of α. Its solution is

$$\int_{298}^{T} \alpha(T)dT = \alpha^o (T - 298) - 20\alpha^o \left(\sqrt{T} - \sqrt{298} \right). \tag{S7}$$

After the temperature has been accounted for, changes to the expansivity, density and moduli due to changes in pressure must be found. The thermal expansivity as a function of pressure is

$$\alpha(T, P) = \alpha(T)(1 + 2f)^{\frac{-3\delta_T}{2}} \tag{S8}$$

where f is the finite strain. The density at pressure is

$$\rho(f) = \rho(T)(1 + 2f)^{3/2}. \tag{S9}$$

11

The isothermal bulk modulus and shear modulus at pressure and temperature to fourth order in strain is

$$K_T(f) = K_T(T)(1+2f)^{5/2} \left\{ \begin{array}{l} 1 - f\left(5 - 3K_T'\right) + \\ \dfrac{f^2}{2}\left[9K_T(T)K_T'' + \left(3K_T' - 7\right)\left(3K_T' - 5\right)\right] \end{array} \right\}$$

$$\mu(f) = \mu(T)(1+2f)^{5/2} \left\{ \begin{array}{l} 1 - f\left(5 - 3\mu' K_T(T)/\mu(T)\right) + \\ \dfrac{f^2}{2}\left[9\mu'' K_T^2(T)/\mu(T) + 9\mu' K_T(T)/\mu(T)\left(K_T' - 4\right) + 35\right] \end{array} \right\}$$

(S10)

The primes in the above expression denote pressure derivatives. Bina and Helffrich suggest μ'' and K_T'' are of order $1/\mu$ and $1/K_T$ and can be directly substituted into the above expressions, though Hacker and Abers prefer an alternate approximation which is to ignore the terms on the right preceded by f^2.

   The strain is found by solving the equation

$$P = 3K_T(T)f(1+2f)^{5/2}\left\{ 1 - 2\xi f + \frac{f^2}{6}\left[9K_T(T)K_T'' + 4\xi\left(4 - 3K_T'\right) + 5\left(3K_T' - 5\right)\right] \right\} \quad (S11)$$

for f. Whereas Hacker and Abers solve this equation iteratively and ignore the term on the right containing $f^2/6$, We turn this equation into a polynomial and use the Matlab roots function to find a solution for f. We then choose the root that is real and closest to the first order solution

$$f = \sqrt{\frac{\left(P/K_T(T)\right)^2}{9}} \ . \qquad\qquad (S12)$$

This method can be obtained as a matlab function at ftp://mantle.colorado.edu/pub/oliverb/MinVel.m. with mineral database at, ftp://mantle.colorado.edu/pub/oliverb/MinPar.csv.

13
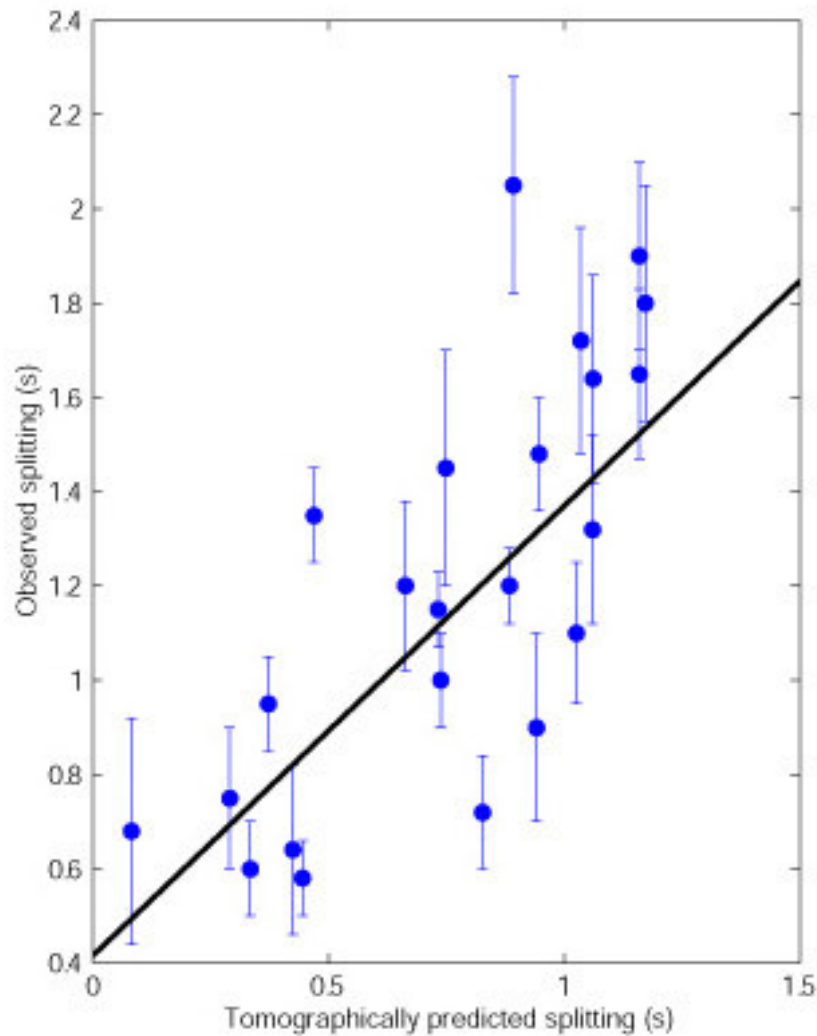
Figure S1. Tomographically predicted shear-wave splitting versus observed SKS splitting. The error bars are standard errors for the SKS splitting measurements. The black line results from a linear regression of the data and has a slope of 0.95 ± 0.1, y-intercept of 0.42 ± 0.07, and linear correlation coefficient of 0.7.

14
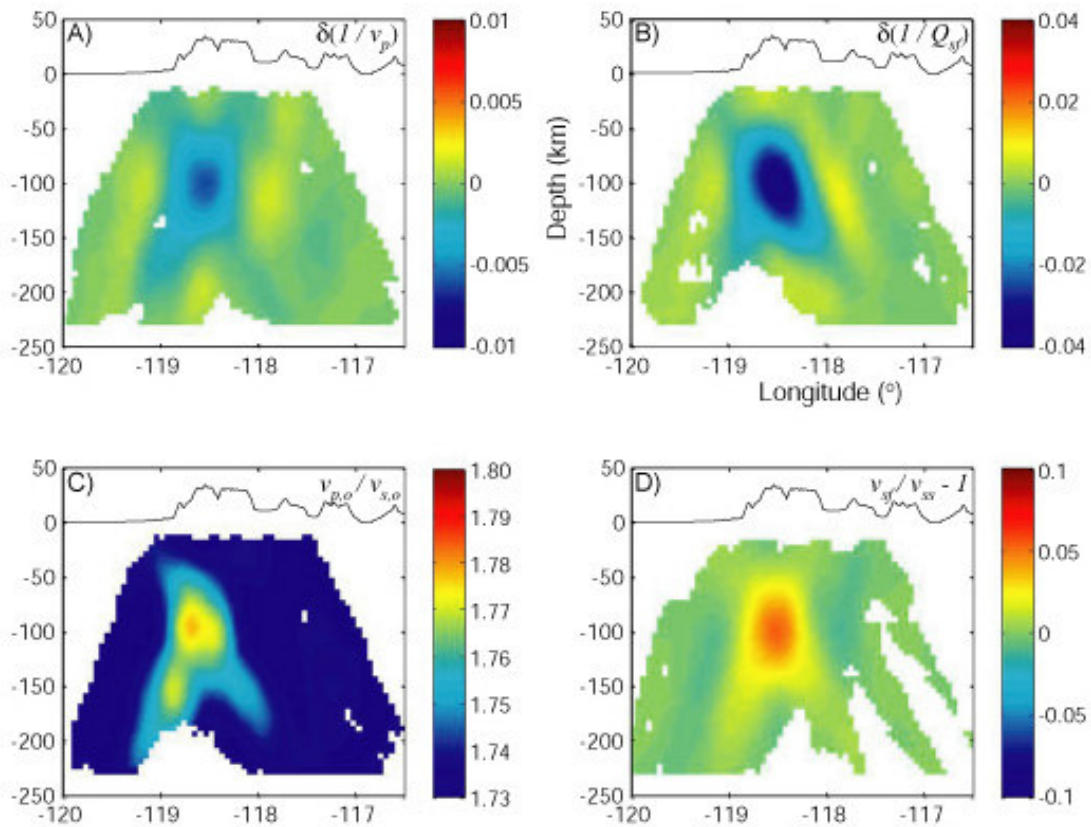
Figure S2. Vertical slices of spike tests at same latitude as figure 2 of main article. 50 km square 'spike' is placed at depth 75 to 125 km, centered about 36.4°N and 118.5°W. A small amount of smearing is present along the ray path directions which are generally oriented NW to SE with a fewer number from the SW and NE. This is in contrast to the EW oriented seismic anomaly presented in figure 2.
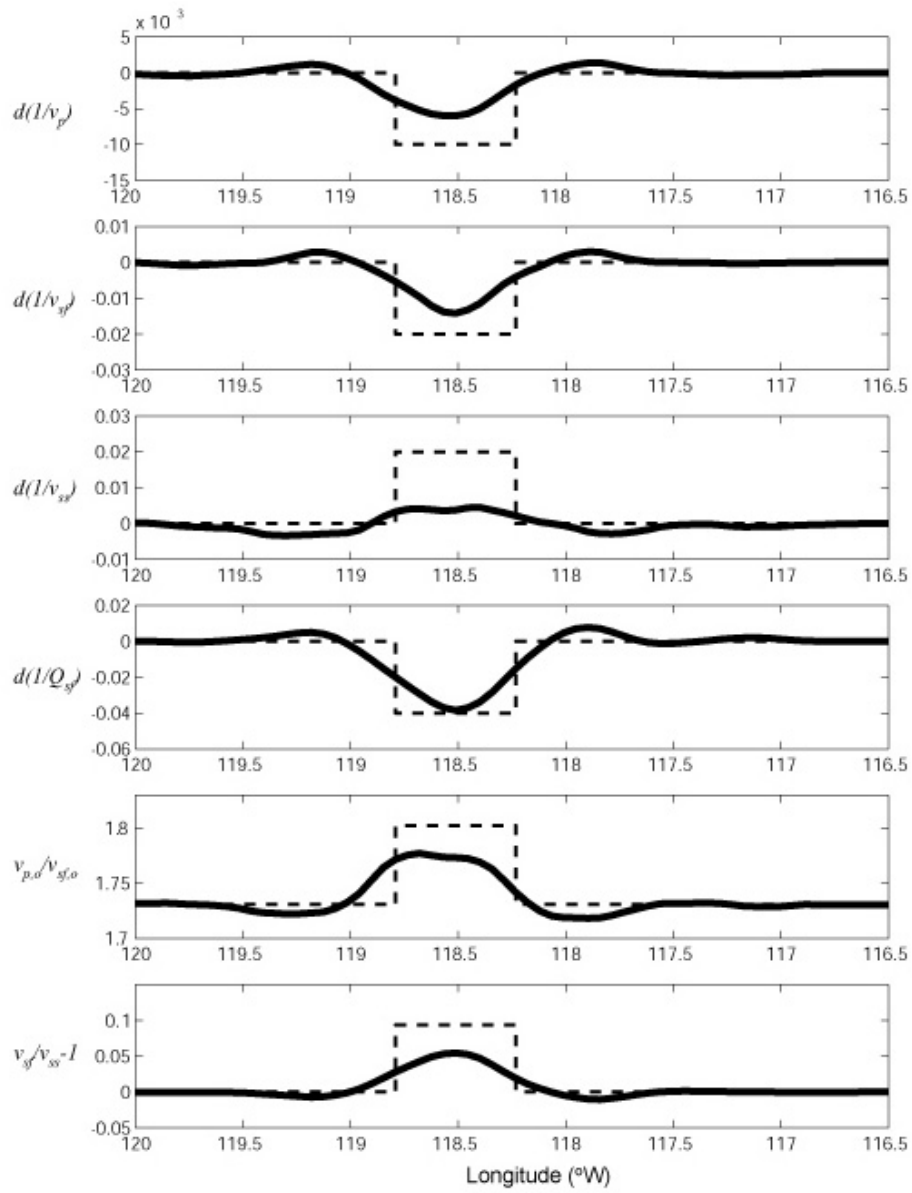
Figure S3. Comparison of spike test results (solid lines) with original spike (dashed lines). From top to bottom is shown $d(1/v_p)$, $d(1/v_{sf})$, $d(1/v_{ss})$, $d(1/Q_{sf})$, $v_{p,o}/v_{sf,o}$ and v_{sf}/v_{ss} -1.

Table S1. Station Information. Station statics result after correcting for elevation.

Name	Longitude	Latitude	Elevation (km)	P	S_{fast}	S_{slow}	S_{fast}	S_{slow}
				wavespeed station static (s)			Δt^* station static (s)	
ARC2	-118.3323	36.0106	2.60	0.162	0.01	0.05	0.3	-0.4
BGR	-119.0166	36.6283	0.95	-0.100	-0.18	-0.23	-0.5	0.0
BPC	-118.4306	37.1282	2.37	0.131	0.44	0.91	0.6	0.4
BRR	-119.0394	36.9127	1.29	0.119	0.14	-0.29	0.0	0.7
BVC	-117.8628	36.7265	0.48	0.281	-0.19	0.40	0.5	0.0
CCC	-118.7868	36.5778	1.56	0.042	0.29	0.60	0.6	0.3
CHP	-118.0919	35.8938	2.43	0.168	0.48	0.37	0.4	-0.2
CPR	-118.5758	36.7967	1.60	-0.233	-0.20	-0.21	0.4	0.1
DP00	-117.6410	36.2670	1.73	0.332	0.14	0.38	0.2	0.4
FLL	-118.9723	37.2798	2.22	0.097	0.60	0.31	0.4	0.3
HVY	-119.3015	36.7200	0.22	-0.325	-0.36	-1.20	0.5	0.3
JUN	-118.4110	36.5810	2.52	-0.050	0.08	0.19	0.7	-0.1
LMC	-119.0291	36.3580	0.23	-0.056	-0.25	-0.12	0.0	0.3
MKW3	-118.6060	36.4540	2.36	0.005	1.51	1.03	0.0	-0.7
OVY	-118.3280	36.7777	2.73	0.005	0.06	-0.04	0.7	-0.1
PDC	-118.9779	36.0333	0.20	-0.087	-0.62	-0.72	0.0	0.0
SFK	-118.8146	36.3656	0.84	0.074	-0.08	-0.23	0.3	0.9
SFT	-118.0627	36.2303	1.83	0.203	0.26	0.18	0.1	0.7
SLC	-117.7175	36.5245	1.94	-0.019	0.05	0.61	-0.4	-1.2
SMD	-118.6302	36.9709	1.81	0.034	-0.37	-0.09	-0.2	0.2
SRF	-118.1060	36.9360	2.18	-0.015	-0.30	0.07	0.3	-0.5
TWR2	-118.4066	36.3513	1.97	-0.011	0.36	-0.03	0.9	0.3
WHP	-118.2216	36.5885	2.42	0.026	0.30	0.32	0.5	0.0
WMD	-118.5749	36.1979	2.67	0.094	0.34	0.14	0.2	-0.4

Table S2. Event information. The last two columns represent the number of stations used for the P and S-wave measurements.

Date	Longitude	Latitude	Depth (km)	Backazimuth (degrees)	Distance (degrees)	P-wave slowness (s/km)	S-wave slowness (s/km)	#P	#S
7/20/97 00:30:21 UTC	-167.5	52.6	14	311.2	37.6	0.076	0.136	22	22
7/20/97 10:14:22 UTC	-66.3	-23.0	256	131.8	77.1	0.050	0.096	21	20
9/02/97 12:13:25 UTC	-75.7	3.9	222	119.5	50.9	0.067	0.123	17	17
9/04/97 04:23:36 UTC	178.3	-26.5	618	233.2	86.7	0.042	0.083	21	21
7/21/97 23:19:39 UTC	-71.9	-30.3	33	140.5	79.8	0.049	0.094	22	22
9/10/97 12:57:10 UTC	-174.4	-21.3	33	232.1	78.3	0.050	0.096	22	22
7/25/97 06:47:03 UTC	-71.8	-30.2	33	140.3	79.8	0.049	0.095	22	22
6/10/97 21:53:55 UTC	-108.1	-35.8	10	171.3	72.9	0.053	0.102	12	11
7/27/97 05:21:29 UTC	-71.8	-30.4	33	140.5	79.9	0.049	0.094	21	21
7/28/97 06:46:55 UTC	142.7	22.3	33	293.2	83.6	0.046	0.090	22	22
6/17/97 21:03:40 UTC	-179.4	51.3	33	309.3	44.9	0.072	0.130	15	12
9/20/97 16:11:32 UTC	-177.6	-28.7	33	229.1	85.7	0.045	0.088	21	22
6/25/97 03:54:12 UTC	-173.2	-15.9	33	235.0	73.6	0.053	0.101	19	15
6/26/97 06:12:09 UTC	-82.5	4.8	10	125.2	45.7	0.071	0.129	19	15
6/26/97 19:21:08 UTC	-114.3	-49.7	10	177.4	86.3	0.044	0.087	19	14
8/08/97 22:27:23 UTC	-179.2	-15.5	33	239.6	77.3	0.050	0.097	21	21
6/27/97 04:39:52 UTC	-26.7	38.3	10	56.9	69.5	0.056	0.106	19	15
8/13/97 04:45:04 UTC	125.8	25.0	55	305.2	93.8	0.041	0.078	20	20
9/30/97 06:27:28 UTC	141.9	32.0	33	301.5	78.5	0.050	0.096	21	21
6/30/97 15:47:39 UTC	-155.1	19.4	8	251.9	36.3	0.077	0.137	19	15
6/30/97 18:56:27 UTC	-80.8	-4.1	33	130.8	53.6	0.066	0.122	19	15
8/15/97 07:37:49 UTC	-105.7	-4.4	10	161.1	42.6	0.073	0.132	20	20
8/17/97 20:11:11 UTC	167.4	-13.7	33	249.6	85.9	0.044	0.088	20	20
8/18/97 12:24:26 UTC	-72.0	-29.9	33	140.3	79.4	0.049	0.095	19	19
10/04/97 15:29:46 UTC	-46.7	15.9	10	87.4	66.1	0.058	0.109	19	0
10/04/97 15:34:29 UTC	-46.8	16.0	10	87.4	65.9	0.058	0.109	19	0
7/05/97 22:46:41 UTC	164.7	-11.5	33	253.0	86.5	0.044	0.087	19	15

7/06/97 09:54:02 UTC	-71.8	-30.1	33	140.2	79.6	0.049	0.095	20	16
7/06/97 20:13:37 UTC	-88.0	16.1	33	119.0	33.8	0.078	0.139	20	16
7/06/97 23:15:20 UTC	-71.9	-30.2	33	140.4	79.7	0.049	0.095	18	17
7/08/97 02:24:07 UTC	142.7	23.8	33	294.3	82.8	0.047	0.091	21	18
7/08/97 12:11:14 UTC	-178.6	51.4	33	309.4	44.4	0.072	0.131	21	18
7/09/97 19:24:11 UTC	-63.6	10.5	10	103.4	55.7	0.064	0.120	21	18
7/10/97 14:55:48 UTC	-70.7	-22.9	33	135.0	74.5	0.052	0.100	21	19
7/14/97 16:09:35 UTC	146.4	43.3	33	309.1	69.3	0.056	0.106	21	18
8/28/97 11:10:07 UTC	-33.9	57.1	10	40.0	57.2	0.064	0.118	20	20
7/15/97 11:15:24 UTC	122.4	24.8	101	307.2	96.1	0.041	0.077	21	0
10/14/97 09:53:18 UTC	-176.8	-22.0	167	233.2	80.4	0.048	0.093	6	6
8/29/97 06:53:59 UTC	-175.7	-15.2	33	237.4	74.8	0.052	0.100	19	19
7/19/97 12:22:57 UTC	-71.4	-29.0	26	139.4	79.0	0.049	0.095	21	21
7/19/97 14:24:23 UTC	-98.2	15.8	33	133.7	27.4	0.088	0.141	21	21

References

S1.   J. Polet, H. Kanamori, *Geophys. J. Int.* **149**, 313 (2002).

S2.   O. S. Boyd, A. F. Sheehan, in *AGU Monograph: Lithospheric Structure and Evolution of the Rocky Mountain Region* K. E. Karlstrom, G. R. Keller, Eds. (in Press).

S3.   S. P. Grand, D. Helmberger, *Geophys. J. Int.* **76**, 399 (1984).

S4.   M. M. Fliedner, S. L. Klemperer, N. I. Christensen, *J. Geophys. Res.* **105**, 10899 (2000).

S5.   J. B. Minster, D. L. Anderson, *Philosophical Transactions of the Royal Society of London Series a-Mathematical Physical and Engineering Sciences* **299**, 319 (1981).

S6.   S. Karato, *Geophys. Res. Lett.* **20**, 1623 (1993).

S7.   W. C. Hammond, E. D. Humphreys, *J. Geophys. Res.* **105**, 10975 (2000).

S8.   S. Karato, H. Jung, *Earth and Planetary Science Letters* **157**, 193 (1998).

S9.   N. I. Christensen, *J. Geophys. Res.* **101**, 3139 (1996).

S10.   W. C. Hammond, E. D. Humphreys, *J. Geophys. Res.* **105**, 10987 (2000).

S11.   B. R. Hacker, G. A. Abers, S. M. Peacock, *J. Geophys. Res.* **108**, 2029, doi:10.1029/2001JB001127 (2003).

S12.   M. Kumazawa, O. L. Anderson, *J. Geophys. Res.* **74**, 5973 (1969).

S13.   V. Babuska, J. Fiala, M. Kumazawa, I. Ohno, Y. Sumino, *Phys. Earth Planet. Inter.* **16**, 157 (1978).

S14. K. S. Aleksandrov, T. V. Ryzhova, B. P. Belikov, *Sov. Phys. Crystallogr.* **8**, 738 (1963).

S15. Y. Gueguen, A. Nicolas, *Annu. Rev. Earth Planet. Sci.* **8**, 119 (1980).

S16. C. R. Bina, G. R. Helffrich, *Annu. Rev. Earth Planet. Sci.* **20**, 527 (1992).

S17. T. J. B. Holland, R. Powell, *J. Meta. Petr.* **16**, 309 (1998).

S18. B. R. Hacker, G. A. Abers, *Geochem. Geophys. Geosys.* **5**, doi:10.1029/2003GC000614 (2004).

Supporting Online Material

www.sciencemag.org

Materials and Methods

Figs. S1, S2, S3

Tbls. S1, S2